

Holocene tephrochronology of Kerguelen Archipelago, Subantarctic Indian Ocean

Fabien Arnaud¹, Pierre Sabatier¹, Anouk Leloup¹, Aymerick Servettaz^{1,2}, Bertrand Moine³, Anne-Lise Develle¹, Stéphane Guédron⁴, Vincent Perrot⁴, Cécile Pignol¹, Jérôme Poulenard¹, Bernard Fanget¹, Emmanuel Malet¹, Eivind Storen⁵, Jean-Louis Reyss^{1,2}, Nicolas Le Viavan⁶, Katrien Heirman⁷, Marc De Batist⁷, Elisabeth Michel², Jacques-Louis de Beaulieu⁸, Nathalie Van der Putten², Jostein Bakke⁵

1) Univ. Grenoble Alpes, Univ. Savoie Mont Blanc, CNRS, EDYTEM, 73000 Chambéry, France

2) Laboratoire des Sciences du Climat et de l'Environnement (LSCE), CEA, CNRS, 91 Gif-sur-Yvette3 : Laboratoire Magmas et Volcans, Université Jean Monnet, CNRS, 42023 Saint-Etienne France

4) Univ. Grenoble Alpes, Univ. Savoie Mont Blanc, CNRS, IRD, IFSTTAR, ISTERre, 38000 Grenoble, France Institut des Sciences de la Terre (ISTerre), Université Grenoble Alpes, CNRS, Grenoble, France

5) Department of Earth Science and Bjerknes Centre for Climate Research, University of Bergen, Allégaten 41, 5007 Bergen, Norway

6) Institut Paul-Emile Victor, 29280, Plouzané, France

7) Renard Centre of Marine Geology, Department of Geology, Ghent University, Krijgslaan 281 S8, B-9000 Ghent, Belgium

8) TNO – Geological Survey of the Netherlands, Princetonlaan 6, NL-3584 CB Utrecht, Netherlands

9) Institut Méditerranéen de Biodiversité et d'Ecologie marine et occidentale (IMBE), Aix-Marseille Université, CNRS, 13545 Aix en Provence, France

10) Department of Earth Sciences, VU University Amsterdam, De Boelelaan 1085, 1081 HV, Amsterdam, the Netherlands

Abstract

Up to now, no geochemical or geochronological data has been published about Holocene volcanic activity on the Kerguelen Archipelago. Here we present the first continuous Holocene chronology of volcanic eruptions on the archipelago. We compared sedimentological, geochronological and geochemical data from two lake sediment cores taken in two different depocenters of Lake Armor, located ca. 70 km away from the archipelago's main volcanic area. This allowed us to confidently assign the pumice- and ash-rich layers that are interbedded in the lake sediments to distinct volcanic eruptions. Eight main and 3 minor eruptions were thus documented and dated, among which the youngest occurred during the Middle Ages, in AD 1020 +/- 58. The oldest eruption (11,175 +/- 275 cal. BP) is also by far the strongest and deposited, more than 1.2 m of up to 3 cm-large pumices in Lake Armor area. The new tephrostratigraphy presented here may serve as a tool to synchronise paleoenvironmental records from Kerguelen as well as marine records from the Kerguelen rise and beyond. areas.

Keywords

Kerguelen, Lake sediments, Tephrostratigraphy, Subantarctic Indian Ocean

50 **Introduction**

51
52 Kerguelen Archipelago is located in the sub-Antarctic Indian Ocean, several thousands of
53 kilometres away from any continental landmass (Fig. 1). Its location in the vicinity of the
54 current position of the subpolar front and within the southern westerly wind belt, makes it
55 particularly sensitive to global climate change and thus a potential key place for climate
56 reconstruction. Moreover, high-quality, millennial-long scale palaeoecological and
57 paleoclimatological records are still scarce in this part of the world (Oppedal et al., 2018;
58 Saunders et al., 2018; Shulmeister et al., 2004; van der Bilt et al., 2017; Van der Putten et al.,
59 2004, 2008, 2015). This makes Kerguelen a potential key target for paleoenvironmental
60 reconstructions such as changes in oceanic and atmospheric circulation patterns (e.g. Sijp and
61 England, 2009). Kerguelen's main island and its dozens of surrounding isles and islets, host a
62 myriad of lakes and peatbogs, holding a great potential for reconstructions of past climate and
63 environment (Arnaud et al., 2016). Lakes in particular are numerous and present a great
64 variety of settings, ranging from small ponds suitable for aDNA (Ficetola et al., 2018) and
65 biomarker palaeothermometry (e.g. Peterse et al., 2014), alpine proglacial lakes that may
66 serve for glacier reconstruction (Dahl et al., 2003; L. T. Oppedal et al., 2018) to fjord-type
67 lakes with large catchments and river systems suitable for paleohydrological reconstructions
68 (Arnaud et al., 2012; Debret et al., 2010; Wessels, 1998). Paleoenvironmental information is
69 particularly robust when such multi-proxy records from different types of lakes are
70 comparable within a precise chronological framework. The restricted vegetation and, in
71 consequence, paucity of terrestrial organic carbon in alpine lake sediments makes the use of
72 radiocarbon dating challenging. It is hence crucial for further studies to establish a common
73 time-scale with ubiquitous tie markers identifiable at least at the archipelago scale. The
74 volcanic nature of the Kerguelen Archipelago, together with indications of recent volcanic
75 activity, makes it possible to use tephrostratigraphy to construct such a chronological
76 framework for correlating different proxy-records (Fontijn et al., 2016; Oppedal et al., 2018).

77
78 Present-day geothermal activity is evidenced by the presence of fumaroles and hot springs on
79 the Rallier Du Baty Peninsula (Fig. 1), in the South-Western part of Kerguelen's main island.
80 Indeed, the most recent evidence of volcanism was found on the Rallier du Baty Peninsula
81 and dated at 26 ± 3 ka BP (Gagnevin et al., 2003). Field observations suggest the existence of
82 more recent volcanic activity as ash and pumice layers of variable thickness were found in
83 peat deposits (Roche-Bellair, 1976; Van der Putten et al., 2015). However, until now no
84 Holocene volcanic deposits have been directly dated and published except for a trachyte of
85 the "Dôme Carva" volcano complex, which was Ar/Ar-dated at about 10 ka (Ethien et al.,
86 2003).

87
88 Here, we present results from the study of two sediment cores from Lake Armor, on
89 Kerguelen's main island (Fig. 1). Both cores contain several well-marked pumice or ash
90 layers. We particularly address the question whether the ash layers are the result of a
91 contemporaneous volcanic eruption or of post-eruptional remobilisation and re-deposition.
92 Every volcanic event deposit is given an age based on radiocarbon dating and the individual
93 layers are geochemically characterised resulting in the first Holocene tephrostratigraphic
94 framework from the Kerguelen Archipelago.

95

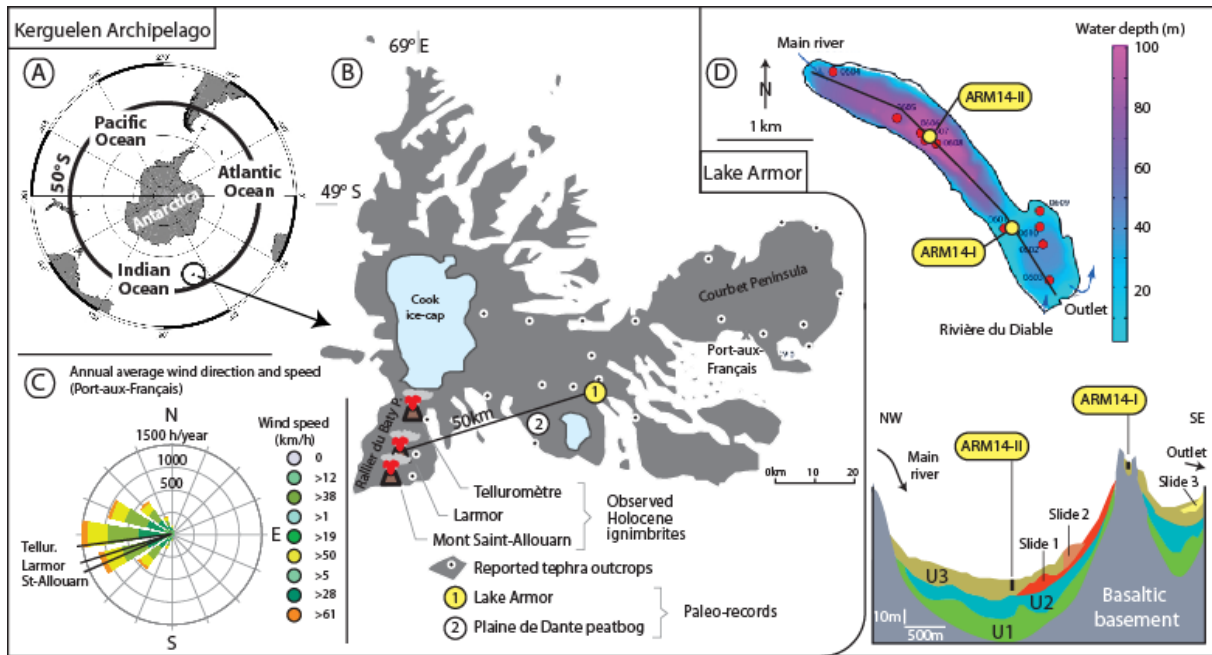


Fig. 1 A: The Southern Ocean with a circle marking the location of the Archipelago Kerguelen located at 49°S in the sub-Antarctic sector of the Indian Ocean. B: Kerguelen with the main geographical features, the location of the Cook Ice cap and the major volcanos in the south. C: Dominant wind speed and direction, recorded at the French research station at Port-aux-Français. D: Lake sediment core locations in Lake Armor, plotted on a bathymetry map and a simplified seismic profile, based on (Heirman et al., 2012).

2. Setting, material and methods

The main island of the Kerguelen Archipelago has a surface area of *ca.* 7215 km². It is the emerged part of the Kerguelen-Gaussberg Oceanic Plateau, which was formed by a series of giant basaltic eruptions *ca.* 40 Ma ago when the SE Indian Ridge (SEIR) overlapped the Kerguelen mantle plume. Since 25 Ma the SEIR migrated to the north but hot spot-type volcanism remained active, due to the persistence of the mantle plume (Ethien et al., 2003). Through time, the magmatic activity decreased leading to differentiation processes and a shift toward a more explosive volcanism. Large volcano-plutonic massifs of syenite and trachyte have hence developed during the last 15 Ma in the south-western province of Kerguelen (Gagnevin et al., 2003). Until recently, the youngest volcanic edifice of the island was thought to be the Mont Ross – the highest summit of Kerguelen – which was active between 1 Ma and 130 ka (Weis et al., 1998).

Lake Armor is located on Kerguelen's main island, 50 km north-east and downwind from the main volcanic edifices on Rallier du Baty Peninsula (Fig. 1). The lake is located 5m asl, is 4 km long and 500 m wide and separated from the sea by a bedrock sill. Bathymetric and seismic surveys were conducted in 2006 and revealed two sub-basins – 100 and 50 m deep – separated by a 20-m-deep rock-sill (Fig. 1), probably of glacial origin (Heirman et al., 2012). A small isolated depocenter on top of this rock-sill records only the air-borne fraction of allochthonous input, whereas the deeper sub-basins record also river-borne sediments, primarily from the main inlet in the north-western end of the lake. Seismic imaging revealed a post-glacial infilling in which 3 units could be recognised (Fig. 1). NW-facing slopes of the central rock-sill seem instable as they are marked by the presence of two underwater landslides.

In 2006, ten short cores were collected from the two main sub-basins, as well as from the small perched depocenter on the sill, using an UWITEC gravity corer. Based on the results of the coring survey and on seismic imagery (Heirman et al., 2012), two sites were selected for

131 retrieving longer cores. These were taken in 2014 using an UWITEC platform and different
132 piston corers. Despite the particularly harsh weather conditions, several cores were collected
133 on each site (Arnaud et al., 2016), giving the opportunity of choosing the optimal cores for
134 tephrochronology and banking material for further studies. From site I (49,4648°S,
135 69,7137°E), a modified Nesje-type corer (Nesje, 1992) designed and built up on the field
136 from parts of an UWITEC Usinger-modified piston corer, was used to take the single run 6.1
137 m long ARM14-I-04 core, which was subsequently split into four sections (S1). From site II
138 (49,45675°S, 69,70193°E), the ARM14-II-03 core was obtained as a composite of a 4 m
139 Nesje-type core (subsequently split into 3 sections), and completed in the same hole by two
140 runs of a 2-m-long UWITEC Niederreiter-type piston corer. Unfortunately, on site II, the
141 sediment below 4 m depth was made of particularly loose non-compacted sand and *ca.* 80 cm
142 were lost at the bottom of each of those runs. The sequence hence reached *ca.* 7.2 m but was
143 fully recovered only down to 4 m, with two additional floating sequences between *ca.* 4 to 5.1
144 m and 6 to 7.2 m (S1).

145 The cores were split into two halves at the EDYTEM laboratory. Each half-section was
146 described in detail and pictures were taken. Lithological description of the sequence allowed
147 the identification of different sedimentary facies.

148
149 X-Ray Fluorescence (XRF) core-scanning was performed for the entire composite sequence
150 with a step size of 5 mm and 0.5 mm for ARM14-I and ARM14-II, respectively, using an
151 Avaatech core-scanner (EDYTEM). X-ray were generated with a Rh anode and geochemical
152 data were obtained with two voltage settings: 10 kV and 1 mA for 20 s for Al, Si, S, K, Ca,
153 Ti, Mn, and Fe and 30 kV and 0.75 mA for 30 s for Cu, Zn, Br, Sr, Rb, Zr, and Pb (Richter et
154 al., 2006). Each individual power spectrum was converted by a deconvolution process into
155 relative components (intensities) expressed in counts per second.

156
157 Sediment core ARM14-I-04 was then subsampled by slicing every 0.5 to 2 cm, depending on
158 the sedimentary facies, in total 591 samples. The dry bulk density (DBD) of each sample was
159 obtained from difference in weight (wet vs dry) after freeze-drying. The 591 sampled volumes
160 were between 1 and 5.5 cm³ and densities vary between 0.17 to 1.18 g.cm⁻³. Each sediment
161 slice was then ground (< 63 μm) using agate mortars for further chemical analysis. For each
162 sample, total Hg concentration (THg) was determined by atomic absorption
163 spectrophotometry following dry mineralization and gold amalgamation using an automatic
164 mercury analyzer [Altec, model AMA 254 (Guédron et al. 2009)]. Quality control for THg
165 analysis was performed by periodic measurements of blanks (n=73), certified reference
166 materials [CRMs: IAEA-158 (n=26), NRCC MESS-3 (n=40) and BCR-679 (n=5)], and
167 sample replicates (n=48). The measurement error was 6.2 % on average and always below 10
168 %. THg was quantified introducing 100 to 200 mg of dry weight sample, leading to a mass of
169 Hg between 0.6 to 40 ng, while the detection limit was 55 pg of Hg (3SD of blank) and the
170 quantification limit was 185 pg of Hg (10SD of blank). The 3 CRMs showed excellent
171 recoveries with values of 128.1 ± 6.2 ng g⁻¹ (certified value = 132 ± 14 ng g⁻¹) for IAEA-158,
172 92.9 ± 2.3 ng g⁻¹ (certified value = 91 ± 9 ng g⁻¹) for MESS-3, and 6.9 ± 0.6 ng g⁻¹ (certified
173 value = 6.3 ± 1.4 ng g⁻¹) for BCR-679. Measurement error on sample replicates ranged from
174 0.03 to 5.38 %.

175
176 Eleven samples of glass shards and pumice layers were selected for major element analysis of
177 glass with an electron microprobe CAMECA© SX100 (Magmas & Volcanoes Laboratory in
178 Clermont-Ferrand, France). Tephra samples were embedded in epoxy resin, polished and
179 carbon metallized. Specific setting for glass analysis was used (low current intensity 5 nA, 15

180 keV, long count for Na and K- 60 s, and background after peak measurement). Only 8 over
181 the 11 samples yielded statically acceptable results.

182

183 Laser Ablation coupled with an ICP-MS was used to analyse the trace and rare earth elements
184 (REE) composition of three samples of glass shards and pumices (also at Magmas &
185 Volcanoes Laboratory in Clermont-Ferrand). The equipment used was an excimer laser
186 system 193 nm Resonetics M-50E, completely computer-controlled and equipped with a laser
187 ATL ultra short pulse duration (< 4 ns), coupled to an ICP-MS spectrometer Agilent 7500
188 with an optical "cs" high sensitivity and a strengthened pump interface. Reproducibility and
189 accuracy of the analyses was estimated through repeated analyses of BCR-2g standard at the
190 beginning and at the end of each run. Data reduction was carried out with the software
191 package GLITTER (Macquarie Research Ltd, 2001 ; van Achterbergh et al., 2001). For each
192 analysis, the time-resolved signal for each element was monitored to discard perturbations
193 related to inclusions, fractures or mixing.

194

195 The upper 10 cm of core ARM14-II were sampled every 5 mm for short-lived radionuclide
196 measurements, using high-efficiency, very low-background, well-type Ge detectors at the
197 Modane Underground Laboratory (LSM) (Reyss et al., 1995). Counting times of 24 to 48
198 hours were required to reach a statistical error of less than 10 % for excess ^{210}Pb in the
199 deepest samples and for the ^{137}Cs peak. In each sample, the ^{210}Pb excess activities ($^{210}\text{Pb}_{\text{ex}}$)
200 were calculated by subtracting the ^{226}Ra -supported activity from the total ^{210}Pb activity.

201

202 Twelve and 14 samples of plant macro-fossils were taken from ARM14-I and ARM14-II,
203 respectively, for AMS radiocarbon dating. Radiocarbon content was measured at the
204 Laboratoire de Mesure 14C (LMC14) ARTEMIS at the CEA (Atomic Energy Commission)
205 institute at Saclay (samples referenced with the prefix Sac in Tab 1) and at the Poznan
206 Radiocarbon Laboratory (samples referenced with the prefix Poz in Tab 1). Remains of
207 terrestrial plants were preferred, except in core ARM14-I, which did not contain any, and for
208 which radiocarbon dating was done on aquatic plant fragments. However, as there is no
209 carbonate in the catchment, we do not expect any significant reservoir effect. Radiocarbon
210 ages were calibrated using the SHcal04 calibration curve (McCormac et al., 2004). Then, we
211 used "clam" (version 3.0.2), the R-based (R Development Core Team, 2011) algorithm
212 developed by Blaauw (2010), to generate an age/depth model.

213

214

215 **3. Results and discussion**

216

217 **3.1. Core description and lithology**

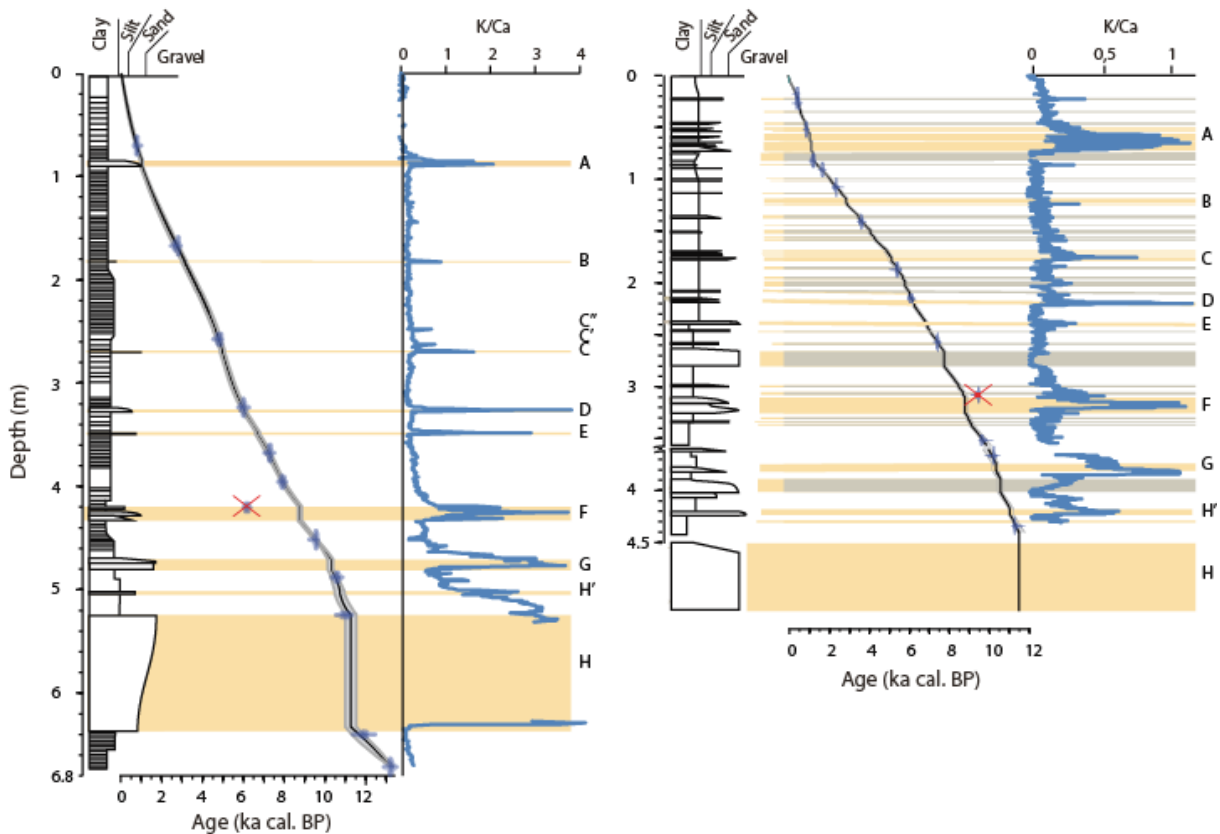
218

219 On site ARM14-I, the sediment consists of a brownish fine mud (Fig. 2), rich in plant
220 remains. This is consistent with field observations of large bryophytes living at the bottom of
221 the lake in this shallow sub-basin (20 m). The continuous sedimentation is interrupted by nine
222 mineral-rich layers, with grainsize ranges from fine silt up to >1 cm gravels. Seven of those
223 layers contain white mm- to cm-large pumices. The most outstanding feature is a thick
224 pumice layer located between 5.25 and 6.35 m below the lake floor. This layer have an
225 inverse grading, which is typical for sub-aquatic pumice deposits, as larger pumices float
226 better than smaller ones and thus sink later following the pumice rain (e.g. Ikehara, 2015).
227 Visible ash and pumice identified in core ARM14-I were labelled from top to bottom, from A
228 to H. The pumice layer identified at 5 m was labelled H' as it is not clear, according to the

229 stratigraphic description, whether it is an individual event or a sub-event following the main
230 pumice-deposit event (H).

231
232 Site ARM14-II presents the same facies of continuous sedimentation as ARM14-I, but with a
233 more complex stratigraphy in terms of interbedded deposits. Indeed, in addition to ash and/or
234 pumice layers, several mm- to cm-thick mineral-enriched fine silt layers are also present.
235 Moreover, the number of pumice layers is higher here than in ARM14-I. Because of this
236 complexity it is not straightforward to correlate both sequences. However, two outstanding
237 features can be recognized: i) the uppermost pumice and ash sequence (85-90 cm in ARM14-
238 I; 50-65 cm in ARM14-II), and ii) the lowermost thick and coarse pumice layer. For both
239 features, deposits in ARM14-II appear to be more complex than those in ARM14-I. The
240 higher number of pumice layers in ARM14-II suggests that this site is submitted to sediment
241 remobilisation and re-deposition. Considering the shape of the lake and the available seismic
242 data (Fig. 1), this sediment reworking may originate from the northern flank of the central
243 rock-sill – at the top of which ARM14-I was taken – or from the main river delta (Heirman et
244 al., 2012).

245



246
247 Fig. 2: Stratigraphic description, age model and K/Ca ratio for the ARM14-I (left) and ARM14-II (right) cores.
248 Rejected ^{14}C ages are identified by a red cross, see table 1. Letters on the right part of each panel are identified
249 tephra layers. Yellow stripe highlight layers interpreted as tephra deposits. Grey stripes highlight ARM14-II
250 layers interpreted as *a posteriori* volcanic material reworking.

251

252 3.2 Chronology

253

254 A logarithmic plot of ($^{210}\text{Pb}_{\text{ex}}$) activities for ARM14-II (SI2) shows a linearly decreasing
255 trend. According to the constant flux, constant sedimentation rate (CFCS) model (Goldberg,
256 1963), using the 'serac' R package (Bruel and Sabatier, 2020), the mean accumulation rate is
257 $1.068 \pm 0.070 \text{ mm.y}^{-1}$ for the upper 10 cm (SI). The profile of ^{137}Cs (SI2) displays an increase

258 at a depth of 6 cm and a peak between 4 and 5.5 cm. According to other studies from the
 259 Southern Hemisphere, the lower peak corresponds to the first appearance of ^{137}Cs at AD
 260 1955, and the upper, peak to AD 1965 (Arnaud et al., 2006; Ficetola et al., 2018). This
 261 temporal correlation is supported by the ^{241}Am peak at the same depth, which was a result of
 262 the decay of ^{241}Pu in fallout from atmospheric nuclear weapons tests (Appleby, 1991). The
 263 good agreement between the ages derived from the $^{210}\text{Pb}_{\text{ex}}$ -CFCS model, and the artificial
 264 radionuclide peaks provide a well-constrained, continuous age-depth relationship for the
 265 upper 60 cm of ARM14-II (SI2).

266
 267 Vegetal macro-remains were collected for radiocarbon dating from core ARM14-I (12
 268 samples) and ARM14-II (14 samples) (Table 1). Two radiocarbon ages were excluded, one is
 269 too old compared to the others (core ARM14-II), probably due to re-mobilisation and re-
 270 deposition of macro-remains stored in the lake catchment area, and the other too young in
 271 ARM14-I, possibly caused by contamination during sampling (Fig. 2). Events
 272 (=instantaneous sedimentation) such as tephra and reworked layers were removed in both
 273 sequences prior to age-depth modelling. The calculated age-depth relationship was done
 274 using a smooth spline function using the R-based algorithm “clam” (version 2.2; Blaauw,
 275 2010) with integration of the short-lived radionuclide-derived ages for ARM14-II. This age-
 276 depth model was used to date all instantaneous deposits. The vertical bars represent the age of
 277 each event thicker than 5 mm with uncertainties (2σ) resulting from the ^{14}C ages (Fig. 2). The
 278 first 670 cm of ARM14-I and the first 470 cm of ARM14-II covered the last 13 and 11,5 kyr
 279 cal BP, respectively. The event-free sedimentation rate for ARM14-II ranges between 0.16
 280 and 0.83 mm yr^{-1} , with a mean of 0.3 mm.yr^{-1} . For ARM14-I the mean event-free
 281 sedimentation rate is 0.43 mm.yr^{-1} , ranging between 0.14 and 0.83 mm yr^{-1} , below 45 cm
 282 sediment depth, and increases to 1,67 mm.yr^{-1} for the upper 45 cm, probably in relation to the
 283 higher water content of this organic rich sediment.

284

Cores	Samples	MCD (m)	Age BP	Age range cal BP
ARM14I	Poz-77362	0,7	800±40	575-744
ARM14I	SacA42461	1,7	2605±30	2497-2757
ARM14I	SacA42462	2,61	4225±30	4584-4838
ARM14I	Poz-77363	3,27	5200±3,15	5752-5995
ARM14I	SacA42463	3,71	6320±35	7028-7294
ARM14I	Poz-77285	4	7030±40	7709-7932
ARM14I	SacA42464	4,25	5335±35	5943-6188
ARM14I	SacA42465	4,56	8485±45	9320-9535
ARM14I	SacA42466	4,93	9345±45	10297-10653
ARM14I	Poz-77286	5,32	9580±60	10663-11125
ARM14I	poz- 73369	6,57	10200±50	11503-12029
ARM14I	SacA42467	6,89	11320±50	13056-13256
ARM14II	SacA-12202	0,18	360±30	310-467
ARM14II	SacA-9751	0,263	425±60	317-515
ARM14II	Poz-69603	0,52	970±30	772-918
ARM14II	Poz-69604	0,81	1295±30	1075-1268
ARM14II	Poz-89883	0,91	1775±30	1571-1713
ARM14II	Poz-69605	1,08	2355±35	2181-2455
ARM14II	Poz-69606	1,41	3395±35	3479-3691
ARM14II	Poz-69607	1,87	4680±40	5146-5575
ARM14II	Poz-89884	2,14	5340±40	5941-6203

ARM14II	Poz-89885	2,56	6540±40	7311-7496
ARM14II	Poz-89887	3,06	8460±50	9304-9528
ARM14II	Poz-89888	3,51	8720±50	9535-9885
ARM14II	Poz-89889	3,65	9090±50	9941-10373
ARM14II	Poz-89891	4,35	9920±50	11194-11596

Table 1. ¹⁴C ages for ARM14I and ARM14II master cores, in bold ages removed for chronology modelling.

3.3. Identification and age of volcanic-related layers

In order to identify more precisely the occurrence of volcanically triggered deposits, both cores were logged on a XRF core scanner. When compared to surrounding basaltic bedrock, Kerguelen most recent volcanic emissions are enriched in potassium (K) relative to calcium (Ca) (Gagnevin et al., 2003), we thus hypothesised that the ratio K/Ca could be a good proxy for the presence of volcanic-triggered layers, as no carbonates are present in the sediment. The XRF-based chemical stratigraphy of ARM14-I confirms this hypothesis, i.e. each tephra layer identified by visual description shows an increase in K/Ca (Figure 2 and 3). Core logging hence led to identify two cryptotephra, which seem to have followed within some decades to centuries the eruption C and further referred as tephra deposits C' and C''.

We further used high-resolution mercury (Hg) measurements as an additional conformation for the presence of these tephra deposits (Daga et al., 2016; Guédron et al., 2019; Ribeiro Guevara et al., 2010). During volcanic eruptions, the rapid deposition of massive inorganic volcaniclasts (tephras) results in abrupt drops in the Hg concentration profile (down to 0.9 ng g⁻¹) diluting the uninterrupted organic-rich sediment deposits (average THg = 23.7 ± 6.7 ng g⁻¹) that have accumulated Hg from the atmosphere. For all potential volcanically triggered event deposits (even the cryptotephra C' and C''), the Hg profile depicts a pattern that is mirrored compared to the K/Ca profile, and presents 2 to 20 fold decreases in Hg concentration compared to the baseline value of uninterrupted sedimentation (Fig. 4A).

We further used high-resolution mercury (Hg) measurements as an additional conformation for the presence of these tephra deposits. While volcanoes are a major natural Hg source in the environment through the atmospheric emission of gaseous elemental Hg (Bagnato et al., 2011), during volcanic eruptions the rapid deposition of massive inorganic volcaniclasts (tephras) results in abrupt drops in the local Hg concentration profiles (Daga et al., 2016; Guédron et al., 2019; Ribeiro Guevara et al., 2010). This is the case here with the lowest Hg content measured in tephra (down to 0.9 ng g⁻¹), as compared to the uninterrupted organic-rich sediment deposits (average THg = 23.7 ± 6.7 ng g⁻¹) that have accumulated Hg from the atmosphere. For all potential volcanically triggered event deposits (even the cryptotephra C' and C''), the Hg profile depicts a pattern that is mirrored compared to the K/Ca profile, and presents 2 to 20 fold decreases in Hg concentration compared to the baseline value of uninterrupted sedimentation (Fig. 4A). In a future work, high resolution pre- and post-depositional Hg variations will be discussed thoroughly with geochemical proxies and meteorological factors throughout the entire ARM14-I sediment core.

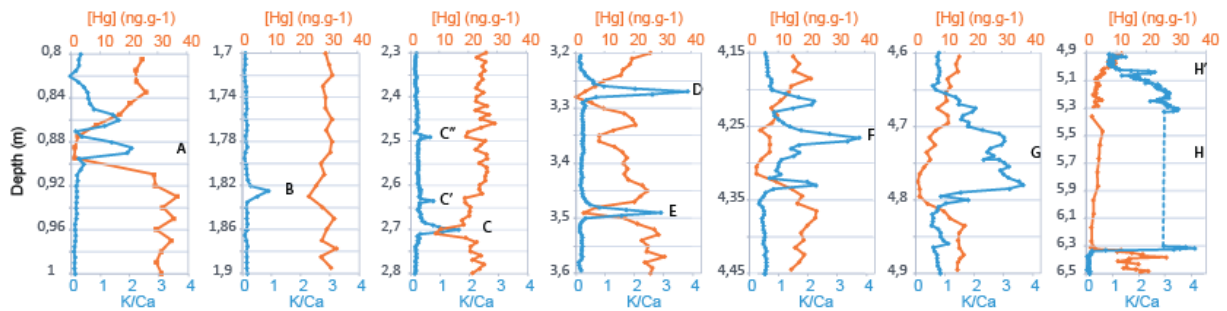


Figure 3. Detection of macro- and cryptotephra deposits using both K/Ca and [Hg] proxies

324
325
326
327
328
329
330
331
332
333
334
335

The chemical stratigraphy combined with independent age-depth models of both cores allowed to determine the event layers that were deposited contemporaneously at both sites (Figures 2 and 3). For this, we applied the following double criterion: i) the presence of a peak in K/Ca, and ii) temporal correlation of similar deposits in both cores. Using this approach, it was possible to correlate all main event deposits in ARM14-I and ARM14-II (Fig. 4). However, in order to assess the intensity of triggering eruptions we used core ARM14-I only because it is solely submitted to direct atmospheric fallout, whereas site II receives input from both direct fallout and river-borne reworked material. Figure 4 shows the thickness of tephra layers and their average grain size.

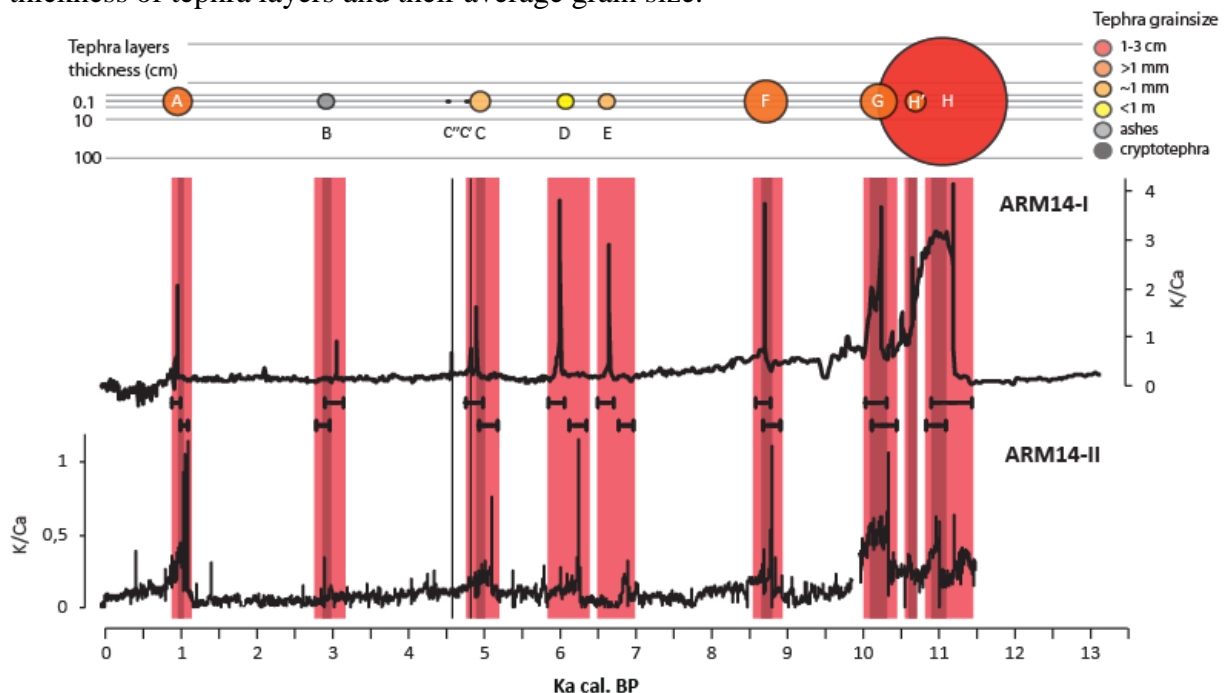


Fig. 4: Synoptic representation of Kerguelen tephrostratigraphy. The upper panel shows the thickness and grain size of tephra in core ARM14-I. The lower panel displays K/Ca ratios in ARM14-I and ARM14-II in relation to age. Light red bands correspond to age uncertainties and dark red bands represent shared age interval in both cores of each tephra layer.

336
337
338
339
340
341
342
343
344
345
346
347
348
349

This analysis leads to the identification of 8 main volcanic eruption events over the last 13,000 years, labelled A to H, from the youngest to the oldest, and 3 smaller events, following shortly after a larger one, labelled C' and C'' (following eruption C) and H' (following eruption H). We note a high recurrence of events in the early Holocene: i.e. ca. 1 event per millennium. These early Holocene events appear also to have been stronger than subsequent events, as they all produced tephra layers of 1 to 10 cm in thickness. Only four weaker events (all in the thickness range of 0.1 to 1 cm, or below) occurred between 1,000 (layer A) and 8,500 ka cal. BP (layer F), i.e. a mean recurrence interval of 1 event every 2 millennia. The

350 very last eruption occurred only ca. 1,000 years ago and brought a pumice layer thicker and
 351 coarser than any of the eruptions since 8,500 ka cal. BP.
 352 X-Ray Fluorescence (XRF) core-scanning was performed for the entire composite sequence
 353 with a step size of 5 mm and 0.5 mm for ARM14-I and ARM14-II, respectively, using an
 354 Avaatech core-scanner (EDYTEM). X-ray were generated with a Rh anode and The
 355 geochemical data were obtained with two tubetwo voltage settings: 10 kV and 1 mA for 20 s
 356 for Al, Si, S, K, Ca, Ti, Mn, and Fe and 30 kV and 0.75 mA for 30 s for Cu, Zn, Br, Sr, Rb,
 357 Zr, and Pb (Richter et al., 2006). Each individual power spectrum was converted by a
 358 deconvolution process into relative components (intensities) expressed in counts per second.
 359 The oldest event has also been the one yielding the most important amount of pumices to
 360 Lake Armor. With more than 1m of deposit without any focusing factor at site I and a
 361 maximum pumice size of several centimetres, it is probable that this event that occurred 70km
 362 away from our study site has been of extreme explosiveness.
 363

Tephra #		A	B	C''	C'	C	D	E	F	G	H'	H
Depth (cm)	Top	85	178	249	263	268,5	328	348	420	472	510	524,5
	Bottom	90,5	179	249	263	270,5	328	349,5	433,5	481	513	633
Age (cal. BP)	min95%	872	2803	4423	4675	4766	5875	6510	8610	10054	10497	10927
	best	944	2950	4559	4805	4894	6003	6649	8705	10246	10737	11191
	max95%	998	3045	4680	4913	4999	6087	6726	8796	10333	10995	11457
Thickness (cm)		6	2	<0,1	<0,1	3	1	1,5	13,5	9	3	109
Visual description		> 1 mm pumices	ash layer	cryptotephra	cryptotephra	~1 mm pumices	<1mm pumices	~1 mm pumices	> 1 mm pumices	> 1 mm pumices	> 1 mm pumices	1-3 cm pumices
Number of microprobe data		3	0	0	4	8	7	0	7	8	7	5
SiO ₂	%	64,78			64,69	62,92	64,16		64,87	64,33	65,28	64,21
	+/- 1 sigma	0,47			0,65	1,10	0,55		1,01	1,21	0,87	0,79
TiO ₂	%	0,36			0,40	0,53	0,46		0,42	0,34	0,31	0,33
	+/- 1 sigma	0,04			0,06	0,09	0,02		0,07	0,03	0,07	0,03
Al ₂ O ₃	%	15,58			15,68	16,50	16,53		15,84	15,76	14,82	15,75
	+/- 1 sigma	0,17			0,75	0,74	0,13		0,89	0,46	1,16	0,34
MgO	%	0,09			0,07	0,26	0,26		0,13	0,10	0,14	0,21
	+/- 1 sigma	0,02			0,09	0,09	0,04		0,07	0,04	0,10	0,02
FeO	%	5,04			4,61	4,94	4,38		4,79	4,45	4,79	4,52
	+/- 1 sigma	0,29			0,22	0,45	0,28		0,16	0,12	0,38	0,14
MnO	%	0,17			0,24	0,22	0,16		0,18	0,18	0,18	0,24
	+/- 1 sigma	0,08			0,13	0,08	0,09		0,12	0,10	0,06	0,06
CaO	%	0,88			0,84	1,18	1,07		0,99	0,88	0,75	0,88
	+/- 1 sigma	0,06			0,19	0,14	0,02		0,24	0,09	0,22	0,05
Na ₂ O	%	6,85			6,80	6,24	6,19		6,45	6,51	6,52	6,24
	+/- 1 sigma	0,05			0,32	0,39	0,19		0,33	0,18	0,34	0,22
K ₂ O	%	5,25			5,44	5,81	5,93		5,39	5,31	5,15	5,55
	+/- 1 sigma	0,13			0,36	0,38	0,12		0,33	0,18	0,48	0,04

364 Tab. 2. List of trachytic volcanic deposits identified in core ARM14-I, with their depth in the core, estimated
 365 age, thickness, visual description and when available, major element concentrations
 366
 367

368 3.4 Geochemical characterisation and origin of tephra deposits

369 The geochemical characteristics of the tephra together with the very close proximity of
 370 trachytes that were described on Rallier du Baty Peninsula confirms their trachytic origin
 371 (Fig. 5A). The hypothesis of a local origin is hence strongly supported. Moreover, the closest
 372 landmasses up-wind are the Crozet Archipelago (1300 km) and the Prince Edward Islands
 373 (2300 km), which did not produce trachytic volcanism.
 374
 375

376 Major element analyses indicate that tephra can be attributed to an alkaline silica-saturated
 377 magmatic series. The concentrations of Na₂O + K₂O and SiO₂ display a very low variability
 378 (Fig 5B). This can be explained, despite an intense fractional crystallization process, by the
 379 fact that the trachytic magma has reached the azeotrope of the alkali feldspars and therefore
 380 the magmatic liquid has the same composition as anorthose, which crystallizes. Only a change
 381 in water activity can allow a change in the major element composition of melts to rhyolitic
 382

383 magmas. Contrarily, the rare earth element (REE) composition displays a significant
 384 variability, illustrating the fractional crystallization process over time in a magma chamber
 385 emptied by successive episodes (Fig. 5A). This is well illustrated by a progressive decrease of
 386 compatible elements, such as Eu, and an increase of highly incompatible elements as other
 387 REE over time.

388
 389 It is not clear yet if all tephra come from the same volcano and/or the same magma chamber.
 390 Indeed, if REEs show an increasing concentration during successive eruptions, this is not the
 391 case for major and minor elements (CaO, TiO₂) of tephra H, which show distinct
 392 compositions. It is quite possible, given the age data already obtained on Rallier du Baty
 393 Peninsula (Ethien et al., 2003), that the most recent tephra come from the eruptive centre of
 394 Mont Saint-Allouarn in the south of the peninsula and that the tephra H comes from another
 395 eruptive centre further north of the peninsula.

396

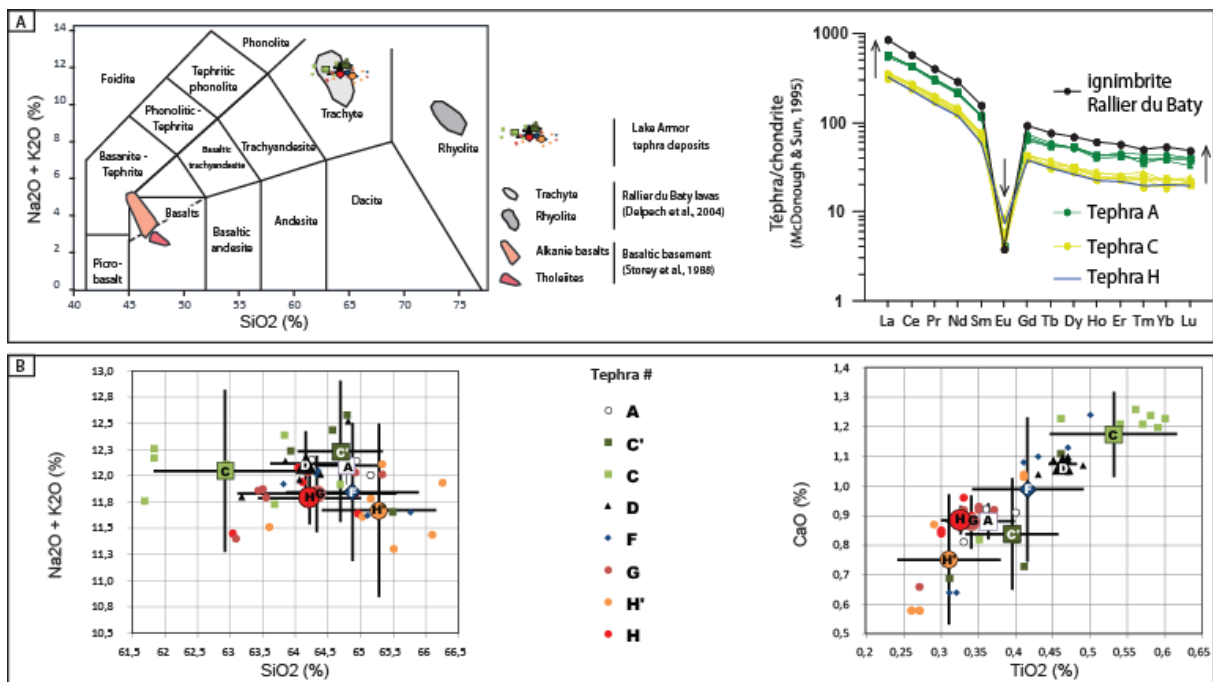


Fig. 5. Geochemical characterisation of Kerguelen tephra deposits. A]

397

398

399

400 Conclusion

401

402 Our first attempt to build a tephrostratigraphic framework for the Kerguelen Archipelago
 403 resulted in a list of 8 main Holocene volcanic events (A, B, C, D, E, F, G and H), to which 3
 404 minor events may be added (C', C'' and H'). Their geochemical composition, as well as their
 405 computed ages are given in Table II. Ongoing studies on cores from several lakes in the
 406 Kerguelen Archipelago will benefit from this first framework, and will allow to synchronise
 407 the records.

408

409 Whereas no evidence of Holocene volcanic activity had previously been published, our results
 410 show eight main Holocene volcanic events (A, B, C, D, E, F, G and H) as well as three minor
 411 events (C', C'' and H') giving a mean return period of one event per millennium. The last
 412 eruption occurred ca. 1,000 years ago and was significantly stronger than any of the eruptions
 413 during the last 8,500 ka cal. BP. The biggest eruption is also the oldest and occurred close to
 414 the onset of the Holocene (11 ka cal. BP). The geochemical composition of the deposits
 415 points to a common origin local source at the Rallier-du-Baty Peninsula SW Kerguelen.

416 Ongoing studies on cores from several lakes in the Kerguelen Archipelago will benefit from
417 this first framework, and will allow robust synchronising of new records.

418

419 **Acknowledgements**

420 We are warmly grateful to IPEV, the French Polar Institute, for providing necessary logistical
421 support for field expeditions (programmes 448-PEISACG, 444-DyLIOKer, 1094-PALAS).
422 Roland Pagni and Dries Boone are warmly thanked for their help on the field. The authors
423 thank the French CNRS-INSU national coring facility and in particular project ANR-11-
424 EQPX-0009-CLIMCOR, for providing coring facilities. Radiocarbon dates referred as SacA
425 were performed at LMC14 facility in Saclay, in the framework of the national programme
426 ARTEMIS. The authors express their grateful thanks to the LMC14 team, in particular to
427 Jean-Pascal Dumoulin, as well as to Tomas Goslar from Poznan Radioacarbon Laboratory for
428 constant help in the management of ¹⁴C samples and results. XRF core scanning was
429 performed thanks at EDYTEM lab as part of the CEMBRO regional analytical facility. The
430 authors thank the Laboratoire Souterrain de Modane (LSM) facilities for the gamma
431 spectrometry measurements and Environnement, Dynamique et Territoires de Montagne
432 (EDYTEM) for the core scanner X-ray fluorescence analyses. This is Laboratory of
433 Excellence ClerVolc contribution n°XXX. The Norwegian contribution was funded by the
434 Norwegian Research Council under the project Shifting Climate States of the Polar Regions
435 (SHIFTS) (project number; 210004).

436

437

438 Appleby, P.G., 1991. 241Am dating of lake sediments. *Hydrobiologia* 214, 35–42.

439 Arnaud, F., Fanget, B., Malet, E., Poulenard, J., Eivind, S., Leloup, A., Jostein, B., Sabatier,
440 P., 2016. Extensive lake sediment coring survey on Sub-Antarctic Indian Ocean
441 Kerguelen Archipelago (French Austral and Antarctic Lands), in: *Geophysical*
442 *Research Abstracts*. Presented at the EGU General Assembly 2016, EGU, Vienne,
443 Autriche, p. 12876.

444 Arnaud, F., Magand, O., Chapron, E., Bertrand, S., Boës, X., Charlet, F., Mélières, M.-A.,
445 2006. Radionuclide dating (210Pb, 137Cs, 241Am) of recent lake sediments in a
446 highly active geodynamic setting (Lakes Puyehue and Icalma—Chilean Lake District).
447 *Sci. Total Environ.* 366, 837–850. <https://doi.org/10.1016/j.scitotenv.2005.08.013>

448 Arnaud, F., Révillon, S., Debret, M., Revel, M., Chapron, E., Jacob, J., Giguet-Covex, C.,
449 Poulenard, J., Magny, M., 2012. Lake Bourget regional erosion patterns reconstruction
450 reveals Holocene NW European Alps soil evolution and paleohydrology. *Quat. Sci.*
451 *Rev.* 51, 81–92. <https://doi.org/10.1016/j.quascirev.2012.07.025>

452 Bagnato, E., Aiuppa, A., Parello, F., Allard, P., Shinohara, H., Liuzzo, M., Giudice, G., 2011.
453 New clues on the contribution of Earth's volcanism to the global mercury cycle. *Bull.*
454 *Volcanol.* 73, 497–510. <https://doi.org/10.1007/s00445-010-0419-y>

455 Blaauw, M., 2010. Methods and code for 'classical' age-modelling of radiocarbon sequences.
456 *Quat. Geochronol.* 5, 512–518.

457 Bruel, R., Sabatier, P., 2020. serac: a R package for ShortlivEd RADionuclide Chronology of
458 recent sediment cores (preprint). *EarthArXiv*. <https://doi.org/10.31223/osf.io/f4yma>

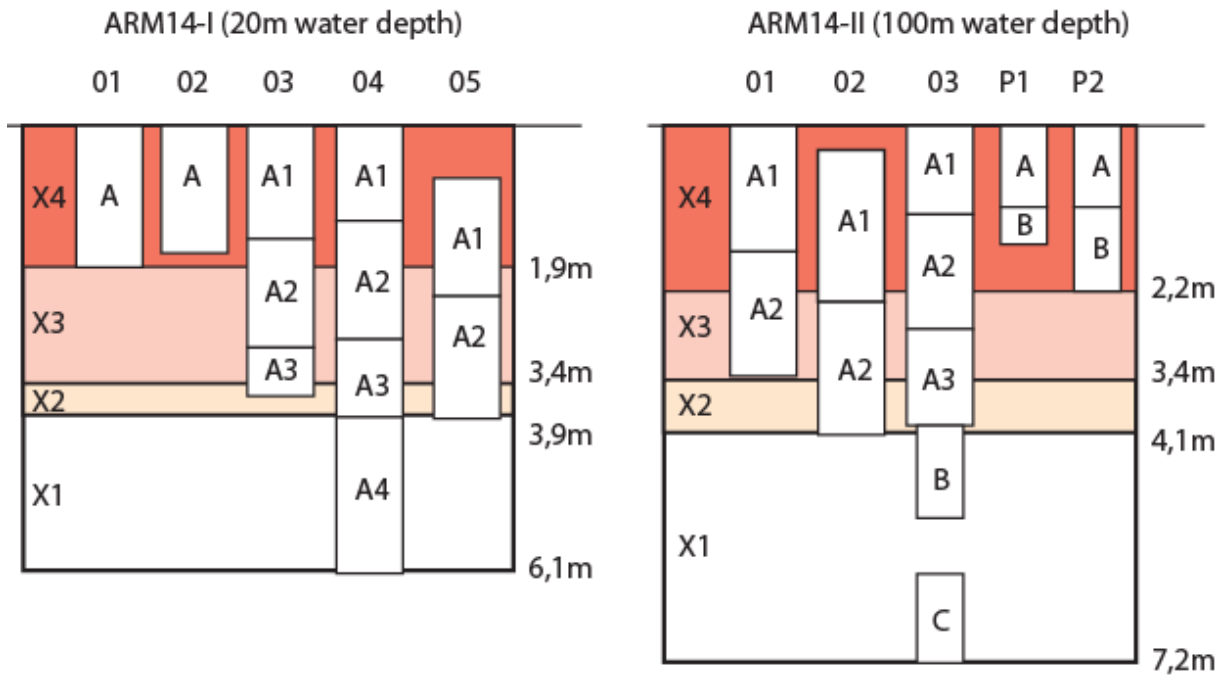
459 Daga, R., Ribeiro Guevara, S., Pavlin, M., Rizzo, A., Lojen, S., Vreća, P., Horvat, M.,
460 Arribère, M., 2016. Historical records of mercury in southern latitudes over
461 1600years: Lake Futalaufquen, Northern Patagonia. *Sci. Total Environ.* 553, 541–550.
462 <https://doi.org/10.1016/j.scitotenv.2016.02.114>

463 Dahl, S.O., Bakke, J., Lie, Ø., Nesje, A., 2003. Reconstruction of former glacier equilibrium-
464 line altitudes based on proglacial sites: an evaluation of approaches and selection of
465 sites. *Quat. Sci. Rev.* 22, 275–287. [https://doi.org/10.1016/S0277-3791\(02\)00135-X](https://doi.org/10.1016/S0277-3791(02)00135-X)

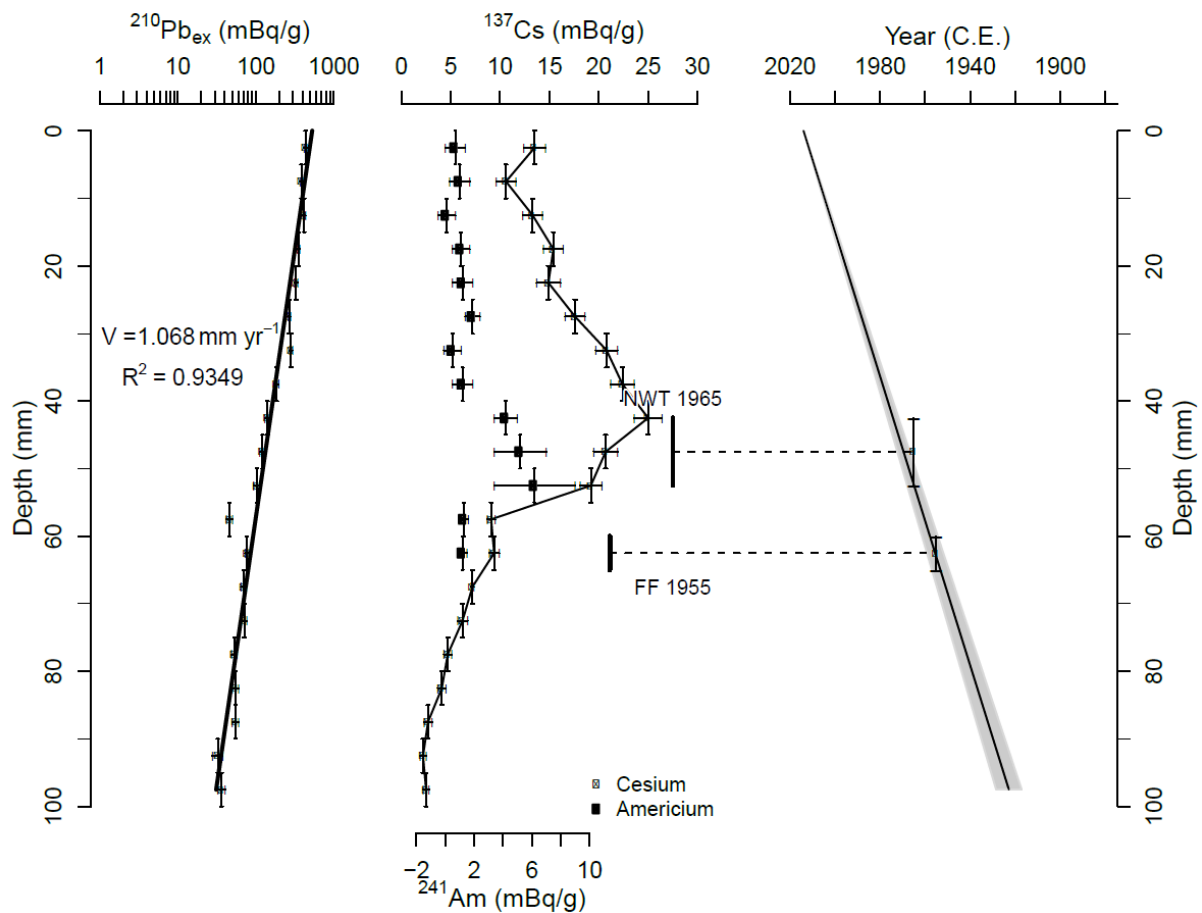
466 Debret, M., Chapron, E., Desmet, M., Rolland-Revel, M., Magand, O., Trentesaux, A., Bout-
467 Roumazeille, V., Nomade, J., Arnaud, F., 2010. North western Alps Holocene
468 paleohydrology recorded by flooding activity in Lake Le Bourget, France. *Quat. Sci.*
469 *Rev.* 29, 2185–2200. <https://doi.org/10.1016/j.quascirev.2010.05.016>
470 Ethien, R., Féraud, G., Gerbe, M.C., Cottin, J.Y., O'Reilly, S.Y., Giret, A., 2003.
471 Geochemistry and Ar/Ar dating of upper pleistocene volcanic rocks from Kerguelen
472 islands (Indian Ocean). Presented at the EGS - AGU - EUG Joint Assembly, p. 6432.
473 Ficetola, G.F., Poulenard, J., Sabatier, P., Messenger, E., Gielly, L., Leloup, A., Etienne, D.,
474 Bakke, J., Malet, E., Fanget, B., Støren, E., Reyss, J.-L., Taberlet, P., Arnaud, F.,
475 2018. DNA from lake sediments reveals long-term ecosystem changes after a
476 biological invasion. *Sci. Adv.* 4, eaar4292. <https://doi.org/10.1126/sciadv.aar4292>
477 Fontijn, K., Rawson, H., Van Daele, M., Moernaut, J., Abarzúa, A.M., Heirman, K., Bertrand,
478 S., Pyle, D.M., Mather, T.A., De Batist, M., Naranjo, J.-A., Moreno, H., 2016.
479 Synchronisation of sedimentary records using tephra: A postglacial
480 tephrochronological model for the Chilean Lake District. *Quat. Sci. Rev.* 137, 234–
481 254. <https://doi.org/10.1016/j.quascirev.2016.02.015>
482 Gagnevin, D., Ethien, R., Bonin, B., Moine, B., Féraud, G., Gerbe, M.C., Cottin, J.Y.,
483 Michon, G., Tourpin, S., Mamias, G., Perrache, C., Giret, A., 2003. Open-system
484 processes in the genesis of silica-oversaturated alkaline rocks of the Rallier-du-Baty
485 Peninsula, Kerguelen Archipelago (Indian Ocean). *J. Volcanol. Geotherm. Res.* 123,
486 267–300. [https://doi.org/10.1016/S0377-0273\(02\)00509-7](https://doi.org/10.1016/S0377-0273(02)00509-7)
487 Goldberg, E.D., 1963. Geochronology with 210Pb, in: *Radioactive Dating*. pp. 121–131.
488 Guédron, S., Tolu, J., Brisset, E., Sabatier, P., Perrot, V., Bouchet, S., Develle, A.L., Bindler,
489 R., Cossa, D., Fritz, S.C., Baker, P.A., 2019. Late Holocene volcanic and
490 anthropogenic mercury deposition in the western Central Andes (Lake Chungará,
491 Chile). *Sci. Total Environ.* 662, 903–914.
492 <https://doi.org/10.1016/j.scitotenv.2019.01.294>
493 Heirman, K., De Batist, M., Arnaud, F., De Beaulieu, J.-L., 2012. Seismic stratigraphy of the
494 late Quaternary sedimentary infill of Lac d'Armor (Kerguelen archipelago): a record
495 of glacier retreat, sedimentary mass wasting and southern Westerly intensification.
496 *Antarct. Sci.* 24, 608–618. <https://doi.org/10.1017/S0954102012000466>
497 Ikehara, K., 2015. Marine tephra in the Japan Sea sediments as a tool for paleoceanography
498 and paleoclimatology. *Prog. Earth Planet. Sci.* 2, 36. [https://doi.org/10.1186/s40645-](https://doi.org/10.1186/s40645-015-0068-z)
499 [015-0068-z](https://doi.org/10.1186/s40645-015-0068-z)
500 McCormac, F.G., Hogg, A.G., Blackwell, P.G., Buck, C.E., Higham, T.F.G., Reimer, P.J.,
501 2004. Shcal04 Southern Hemisphere Calibration, 0–11.0 Cal Kyr BP. *Radiocarbon* 46,
502 1087–1092. <https://doi.org/10.1017/S0033822200033014>
503 Nesje, A., 1992. A Piston Corer for Lacustrine and Marine Sediments. *Arct. Alp. Res.* 24,
504 257. <https://doi.org/10.2307/1551667>
505 Oppedal, Bilt, W.G.M. van der, Balascio, N.L., Bakke, J., 2018. Patagonian ash on sub-
506 Antarctic South Georgia: expanding the tephrostratigraphy of southern South America
507 into the Atlantic sector of the Southern Ocean. *J. Quat. Sci.* 33, 482–486.
508 <https://doi.org/10.1002/jqs.3035>
509 Oppedal, L.T., Bakke, J., Paasche, Ø., Werner, J.P., van der Bilt, W.G.M., 2018. Cirque
510 Glacier on South Georgia Shows Centennial Variability over the Last 7000 Years.
511 *Front. Earth Sci.* 6, 2. <https://doi.org/10.3389/feart.2018.00002>
512 Peterse, F., Vonk, J.E., Holmes, R.M., Giosan, L., Zimov, N., Eglinton, T.I., 2014. Branched
513 glycerol dialkyl glycerol tetraethers in Arctic lake sediments: Sources and implications
514 for paleothermometry at high latitudes. *J. Geophys. Res. Biogeosciences* 119, 1738–
515 1754. <https://doi.org/10.1002/2014JG002639>

- 516 R Development Core Team, 2011. R: a Language and Environment for Statistical Computing.
517 R Foundation for Statistical Computing, Vienna.
- 518 Reyss, J.-L., Schmidt, S., Legeleux, F., Bonte, P., 1995. Large low background well type
519 detectors for measurements of environmental radioactivity. *Nucl Instrum Methods*
520 357, 391–397.
- 521 Ribeiro Guevara, S., Meili, M., Rizzo, A., Daga, R., Arribère, M., 2010. Sediment records of
522 highly variable mercury inputs to mountain lakes in Patagonia during the past
523 millennium. *Atmospheric Chem. Phys.* 10, 3443–3453. [https://doi.org/10.5194/acp-](https://doi.org/10.5194/acp-10-3443-2010)
524 10-3443-2010
- 525 Roche-Bellair, N., 1976. Les variations climatiques de l'holocène supérieur des îles
526 Kerguelen: d'après la coupe d'une tourbière de la plaine de Dante (côte méridionale).
527 *Comptes Rendus Académie Sci. Sér. D* 282, 1257–1260.
- 528 Saunders, K.M., Roberts, S.J., Perren, B., Butz, C., Sime, L., Davies, S., Van Nieuwenhuyze,
529 W., Grosjean, M., Hodgson, D.A., 2018. Holocene dynamics of the Southern
530 Hemisphere westerly winds and possible links to CO₂ outgassing. *Nat. Geosci.*
531 <https://doi.org/10.1038/s41561-018-0186-5>
- 532 Shulmeister, J., Goodwin, I., Renwick, J., Harle, K., Armand, L., McGlone, M.S., Cook, E.,
533 Dodson, J., Hesse, P.P., Mayewski, P., Curran, M., 2004. The Southern Hemisphere
534 westerlies in the Australasian sector over the last glacial cycle: a synthesis. *Quat. Int.,*
535 *Climates, human, and natural system of the PEP II transect* 118–119, 23–53.
536 [https://doi.org/10.1016/S1040-6182\(03\)00129-0](https://doi.org/10.1016/S1040-6182(03)00129-0)
- 537 Sijp, W.P., England, M.H., 2009. Southern Hemisphere Westerly Wind Control over the
538 Ocean's Thermohaline Circulation. *J. Clim.* 22, 1277–1286.
539 <https://doi.org/10.1175/2008JCLI2310.1>
- 540 van Achterbergh, E., Griffin, W.L., Stiefenhofer, J., 2001. Metasomatism in mantle xenoliths
541 from the Letlhakane kimberlites: estimation of element fluxes. *Contrib. Mineral.*
542 *Petrol.* 141, 397–414. <https://doi.org/10.1007/s004100000236>
- 543 van der Bilt, W.G.M., Bakke, J., Werner, J.P., Paasche, Ø., Rosqvist, G., Vatile, S.S., 2017.
544 Late Holocene glacier reconstruction reveals retreat behind present limits and two-
545 stage Little Ice Age on subantarctic South Georgia. *J. Quat. Sci.* 32, 888–901.
546 <https://doi.org/10.1002/jqs.2937>
- 547 Van der Putten, N., Hébrard, J.-P., Verbruggen, C., Van de Vijver, B., Disnar, J.-R., Spassov,
548 S., de Beaulieu, J.-L., De Dapper, M., Keravis, D., Hus, J., Thouveny, N., Frenot, Y.,
549 2008. An integrated palaeoenvironmental investigation of a 6200 year old peat
550 sequence from Ile de la Possession, Iles Crozet, sub-Antarctica. *Palaeogeogr.*
551 *Palaeoclimatol. Palaeoecol.* 270, 179–195.
552 <https://doi.org/10.1016/j.palaeo.2008.09.014>
- 553 Van der Putten, N., Stieperaere, H., Verbruggen, C., Ochyra, R., 2004. Holocene
554 palaeoecology and climate history of South Georgia (sub-Antarctica) based
555 on a macrofossil record of bryophytes and seeds. *The Holocene* 14, 382–392.
556 <https://doi.org/10.1191/0959683604hl714rp>
- 557 Van der Putten, N., Verbruggen, C., Björck, S., Michel, E., Disnar, J.-R., Chapron, E., Moine,
558 B.N., de Beaulieu, J.-L., 2015. The Last Termination in the South Indian Ocean: A
559 unique terrestrial record from Kerguelen Islands (49°S) situated within the Southern
560 Hemisphere westerly belt. *Quat. Sci. Rev.* 122, 142–157.
561 <https://doi.org/10.1016/j.quascirev.2015.05.010>
- 562 Weis, D., Frey, F.A., Giret, A., Cantagrel, J.-M., 1998. Geochemical Characteristics of the
563 Youngest Volcano (Mount Ross) in the Kerguelen Archipelago: Inferences for Magma
564 Flux, Lithosphere Assimilation and Composition of the Kerguelen Plume. *J. Petrol.*
565 39, 973–994. <https://doi.org/10.1093/petroj/39.5.973>

566 Wessels, M., 1998. Natural environmental changes indicated by Late Glacial and Holocene
 567 sediments from Lake Constance, Germany. *Palaeogeogr. Palaeoclimatol. Palaeoecol.*
 568 140, 421–432. [https://doi.org/10.1016/S0031-0182\(98\)00026-1](https://doi.org/10.1016/S0031-0182(98)00026-1)
 569
 570
 571
 572
 573



574
 575 S1. Scheme of different core sections taken in Lake Armor site 14-I (perched basin) and 14-II (deep
 576 basin) during the 2014 PALAS expedition. Background colours reflect the number of sections
 577 available for a given depth, from 4 (X4) to 1 (X1). NB: those depths correspond to measurements
 578 makes on the field, due to further decompression of the sediment, they are slightly different from
 579 model-depths used while referring sample depths in the paper.
 580
 581



582
 583 Figure S2 : From left to right : $^{210}\text{Pb}_{\text{ex}}$ activities, ^{137}Cs and ^{241}Am activities, and the age
 584 model for the upper 10 cm of ARM14 II computed thanks to *serac* R package (Bruel and
 585 Sabatier, 2020).
 586